JOURNAL OF MATERIALS SCIENCE 32 (1997) 5143–5154

Effect of interfacial thickness and stiffness on the stress distributions in fibre reinforced cementitious composites

J. S. HUANG*, M. T. CHEN
Department of Civil Engineering, National Cheng Kung University, Tainan 70101, Taiwan

The different microstructure of the fibre–cement interface might result in different failure mechanisms. It is expected that improvement of strength and toughness in fibre-reinforced cementitious composites will depend on their interfacial thickness and stiffness. A three-phase model, subject to a transversely uniform tensile stress, was utilized to investigate the effect of interfacial thickness and stiffness on the stress distributions near the fibre–cement interface and the corresponding failure mechanism. The results suggest that optimum interfacial microstructure of fibre-reinforced cementitious composites can be tailored to obtain a higher strength and toughness. Optimum interfacial thickness and stiffness was evaluated for various reinforcements, including steel, carbon, glass and polypropylene fibres.

1. Introduction

In general, cement-based materials are brittle and possess a lower value of tensile strength and fracture toughness, due to the nature of their microstructure which includes, among others, pre-existing micro-cracks induced from mixing and curing. The tensile strength and fracture toughness of cementitious materials can be improved by introducing ductile fibres, such as steel fibres, into a cement slurry. The magnitude of the tensile strength and fracture toughness increase of fibre-reinforced cementitious composites is mainly controlled by their microstructural morphology near the fibre–cement interface. To achieve the goal of increasing strength and toughness in fibre-reinforced cementitious composites, the effect of interfacial thickness and stiffness on the stress distributions near fibre–cement interface needs to be fully exploited. It is expected that fibre-reinforced cementitious composites with high tensile strength and fracture toughness can be obtained by tailoring the microstructure of the fibre–cement interface.

Typically, steel or glass fibre is added to a cement slurry to increase the tensile strength and fracture toughness of cementitious composites. Aveston *et al.* [1] found that the applied load is carried by both fibres and cement matrix before any crack is formed. Once an initial crack nucleates and propagates, the force originally exerted on the cement matrix will be transferred to the surrounding fibres through a shear deformation mechanism. Fibres will be ruptured if their tensile strength is relatively low. Otherwise, multiple fracture of the cement matrix is more likely to occur, giving a fibre pull-out failure mechanism. The critical volume fraction of fibres, above which fibre rupture failure can be avoided, was suggested by Ramachandran *et al.* [2]: 0.31% for steel fibres, 0.4% for glass fibres and 0.75% for polypropylene fibres.

The different microstructure of the fibre–cement interface might change the failure mechanism of fibre-reinforced cementitious composites. Bentur *et al.* [3] concluded that the cement paste near a steel fibre/cement interface composed of a lot of CH crystals and with high porosity, differs from the bulk cement paste further away from the steel fibre surface. It was also observed that the cracks initiated within the cement matrix interact with the porous interface, then being deflected and arrested. By using scanning electronic micrography, Mindess and Young [4] learned that crystalline CH possesses a needle-like microstructure. As a result of that, the CH crystals near the fibre–cement interface tend to jostle each other and develop a porous area.

Bentur *et al.* [5] observed that crack propagation in cement paste specimens reinforced with steel fibres could not break the steel fibre directly, but was initially stopped at a distance of 10–40 μm from the fibre surface. Then, the crack was displaced laterally and ran parallel to the fibre surface. By conducting a series of microhardness measurements, Wei *et al.* [6] found that the microhardness of the cement matrix far from the fibre surface tends to be constant, and then drops gradually on approaching the fibre surface. After reaching a minimum value at a distance of about 60 μm from the fibre surface, the microhardness of the cement matrix arise because it is close to the fibre surface. Bentur [7] suggested that control of the microstructure of the fibre–cement interface provides a means for improving the mechanical properties of fibre-reinforced cementitious composites. For example, pozzolanic materials, such as fumed silica,

* Author to whom all correspondence should be addressed.

0022–2461

can be introduced in a cement slurry to make the fibre–cement interface less porous, increasing its interfacial stiffness but decreasing its interfacial thickness. Kawamura and Igarashi [8] verified that the interfacial thickness and stiffness in fibre reinforced cementitious composites were influenced by factors such as cement age and water/cement ratio. In other words, it is possible to tailor the microstructure of the fibre–cement interface to achieve the desired mechanical properties.

Lo *et al.* [9] proposed a four-phase composite cylindrical model to study the effect of interphase modulus and thickness on the stress distributions in the resin matrix. Because the matrix is surrounded by an equivalent composite medium, and the interaction between fibres is taken into account, the four-phase model is only suitable for composites with higher volume fraction of fibres. Based on the results of their analysis, optimal interphase thickness for E-glass fibre-reinforced composites was suggested. Using computer simulation of a discrete grid points model, Monette *et al.* [10] studied the effect of interphase modulus and cohesive energy on the critical fibre length in short-fibre-reinforced brittle composites. They also identified various failure mechanisms as a function of interphase modulus.

The stress distributions near the fibre–cement interface will be influenced by interfacial thickness and stiffness. As a result, different interface microstructure might result in a different failure mechanism and mechanical properties in fibre-reinforced cementitious composites. In most cases of engineering applications, the volume fraction of fibres in cementitious composites is relatively low when construction cost and workability are taken into account. Thus, a dilute solution three-phase model subject to a transversely uniform tensile stress was employed here to study the effect of interfacial thickness and stiffness on the stress distributions near the fibre–cement interface. Selection of optimal interfacial thickness and stiffness for cementitious composites reinforced with various fibres are discussed and compared with each other.

2. Modelling

The stress distributions near the fibre–cement interface play an important role in determining the corresponding failure mechanism and in increasing the magnitude of tensile strength and fracture toughness of fibre-reinforced cementitious composites. Christensen [11] suggested that a dilute solution model can be employed to simulate the stress distributions in fibre-reinforced composites if the volume fraction of fibres is low. In practice, the fibre content in cementitious composites is usually less than 10%; the interaction between fibres can be neglected in modelling. In addition, fibre length is much larger than its radius; the problem can be further simplified to a two-dimensional particulate model equivalent to a three-dimensional cylindrical under plane strain conditions.

The dilute solution three-phase model used in the study is shown in Fig. 1: a single fibre with a radius a, a porous interface with a thickness b measured from the outer surface of the central fibre, and an infinite cement matrix surrounding the fibre and porous interface. For simplicity, a transversely uniform tensile stress at infinity, denoted by σ, is exerted on the outer boundary of the model to evaluate the effect of interfacial thickness and stiffness on the stress distributions near the fibre–cement interface. In polar coordinates, the applied stresses can be expressed as

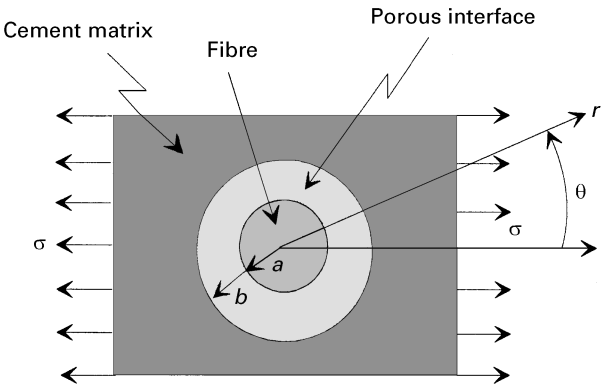

Figure 1 A dilute solution model with a single fibre of radius a and a porous interface of thickness b in a cement matrix.

$$\sigma_r^* = \frac{\sigma(1 + \cos 2\theta)}{2} \tag{1a}$$

$$\sigma_\theta^* = \frac{\sigma(1 - \cos 2\theta)}{2} \tag{1b}$$

$$\sigma_{r\theta}^* = -\frac{\sigma \sin 2\theta}{2} \tag{1c}$$

where σ_r^* is the radial normal stress, σ_θ^* is the circumferential normal stress, $\sigma_{r\theta}^*$ is the shearing stress and θ is the angle. The applied stresses can be divided into two groups: angle-independent normal stresses and angle-dependent normal and shearing stresses. The proposed model under either the angle-independent normal stresses or angle-dependent normal and shear stresses will be analysed, separately. The actual stress distributions near the fibre–cement interface can be obtained from the results of the two applied stress states by using the superposition principle of elasticity.

2.1. Angle-independent applied stresses

For a model under uniform normal stresses, $\sigma_r^* = \sigma_\theta^* = \sigma/2$, the stress and displacement fields within the model were derived by Timoshenko and Goodier [12]

$$\sigma_r = \frac{A}{r^2} + (2 \log r + 1)B + 2C \tag{2a}$$

$$\sigma_\theta = \frac{A}{r^2} + (2 \log r + 3)B + 2C \tag{2b}$$

$$\sigma_{r\theta} = 0 \tag{2c}$$

$$2Gu_r = -\frac{A}{r} + [(2 - 4\nu)r \log r - r]B + (2 - 4\nu)rC \tag{2d}$$

$$2Gu_\theta = B(4 - 4\nu)r\theta \tag{2e}$$

where G and ν are the shear modulus and Poisson's ratio of any phase material, u_r is the radial displacement, u_θ is the circumferential displacement, and r is the radial distance measured from the centre of the model. A, B and C are unknown constants and need to be determined from boundary conditions. Equation 2 is valid for any of the three phases: fibre, porous interface and cement matrix. Hence, there are nine unknown constants in the model: A_1, A_2, A_3, B_1, B_2, B_3, C_1, C_2 and C_3. Nine boundary conditions must be satisfied in the three-phase model: $u_\theta|_{\theta=0}^{r\geqslant a+b} = u_\theta|_{\theta=2\pi}^{r\geqslant a+b}$, $u_\theta|_{\theta=0}^{a\leqslant r\leqslant a+b} = u_\theta|_{\theta=2\pi}^{a\leqslant r\leqslant a+b}$, $u_\theta|_{\theta=0}^{r\leqslant a} = u_\theta|_{\theta=2\pi}^{r\leqslant a}$, $\sigma_r|_{r\to\infty} = \sigma_\theta|_{r\to\infty} = \sigma/2$, $\sigma_r|_{r\to(a+b)^+} = \sigma_r|_{r\to(a+b)^-}$, $u_r|_{r\to(a+b)^+} = u_r|_{r\to(a+b)^-}$, $\sigma_r|_{r\to a^+} = \sigma_r|_{r\to a^-}$, $u_r|_{r\to a^+} = u_r|_{r\to a^-}$ and $u_r|_{r=0}$ = finite value.

The nine unknown constants can be determined from the nine boundary conditions and expressed in terms of material properties and microstructure geometries

$$A_1 = \sigma(1-\nu^m)\frac{G^p}{G^m}\left\{a^2\left[-(2-4\nu^f)\frac{G^p}{G^f} + (2-4\nu^p)\right] + 2(a+b)^2\left[1+(1-2\nu^f)\frac{G^p}{G^f}\right]\right\} \times\left\{\left(\frac{a}{a+b}\right)^2\left[(2-4\nu^f)\frac{G^p}{G^f}-(2-4\nu^p)\right] \times\left(1-\frac{G^p}{G^m}\right)+2\left[\frac{G^p}{G^m}+(1-2\nu^p)\right] \times\left[1+(1-2\nu^f)\frac{G^p}{G^f}\right]\right\}^{-1} - \frac{\sigma}{2}(a+b)^2 \quad (3a)$$

$$A_2 = a^2\sigma(1-\nu^m)\left[(2-4\nu^f)\frac{G^p}{G^f}-(2-4\nu^p)\right]\frac{G^p}{G^m} \times\left\{\left(\frac{a}{a+b}\right)^2\left[(2-4\nu^f)\frac{G^p}{G^f}-(2-4\nu^p)\right] \times\left(1-\frac{G^p}{G^m}\right)+2\left[\frac{G^p}{G^m}+(1-2\nu^p)\right] \times\left[1+(1-2\nu^f)\frac{G^p}{G^f}\right]\right\}^{-1} \quad (3b)$$

$$A_3 = B_1 = B_2 = B_3 = 0 \quad (3c)$$

$$C_1 = \frac{\sigma}{4} \quad (3d)$$

$$C_2 = \sigma(1-\nu^m)\left[1+(1-2\nu^f)\frac{G^p}{G^f}\right]\frac{G^p}{G^m} \times\left\{\left(\frac{a}{a+b}\right)^2\left[(2-4\nu^f)\frac{G^p}{G^f}-(2-4\nu^p)\right] \times\left(1-\frac{G^p}{G^m}\right)+2\left[\frac{G^p}{G^m}+(1-2\nu^p)\right] \times\left[1+(1-2\nu^f)\frac{G^p}{G^f}\right]\right\}^{-1} \quad (3e)$$

$$C_3 = \sigma(1-\nu^m)\frac{G^p}{G^m}\left[-(1-2\nu^f)\frac{G^p}{G^f}+(1-2\nu^p)\right] \times\left\{\left(\frac{a}{a+b}\right)^2\left[(2-4\nu^f)\frac{G^p}{G^f}-(2-4\nu^p)\right] \times\left(1-\frac{G^p}{G^m}\right)+2\left[\frac{G^p}{G^m}+(1-2\nu^p)\right] \times\left[1+(1-2\nu^f)\frac{G^p}{G^f}\right]\right\}^{-1} \quad (3f)$$

where the superscripts f, p and m represent the material properties of fibre, porous interface and cement matrix, respectively. The stress distributions near the fibre–cement interface can be calculated once the unknown constants are found.

2.2. Angle-dependent applied stresses

Timoshenko and Goodier [12] gave the stress and displacement fields of the dilute solution model under uniform angle-dependent normal stresses $\sigma_r^* = \sigma\cos 2\theta/2$, $\sigma_\theta^* = -\sigma\cos 2\theta/2$ and shearing stress $\sigma_{r\theta}^* = -\sigma\sin 2\theta/2$

$$\sigma_r = -\left(2A + \frac{6C}{r^4} + \frac{4D}{r^2}\right)\cos 2\theta \quad (4a)$$

$$\sigma_\theta = \left(2A + 12Br^2 + \frac{6C}{r^4}\right)\cos 2\theta \quad (4b)$$

$$\sigma_{r\theta} = \left(2A + 6Br^2 - \frac{6C}{r^4} - \frac{2D}{r^2}\right)\sin 2\theta \quad (4c)$$

$$2Gu_r = \left[-2Ar - 4\nu Br^3 + \frac{2C}{r^3} + \frac{D(4-4\nu)}{r}\right]\cos 2\theta \quad (4d)$$

$$2Gu_\theta = \left[2Ar + (6-4\nu)Br^3 + \frac{2C}{r^3} - \frac{D(2-4\nu)}{r}\right]\cos 2\theta \quad (4e)$$

Again, G and ν are material properties and A, B, C and D are unknown constants. Equations 4a–e are applicable to fibre, porous interface and cement matrix. Therefore, twelve unknown constants need to be solved in the three-phase model: A_4, A_5, A_6, B_4, B_5, B_6, C_4, C_5, C_6, D_4, D_5 and D_6. Twelve boundary conditions are: $\sigma_r|_{r\to\infty} = -\sigma_\theta|_{r\to\infty} = \sigma(\cos 2\theta)/2$, $\sigma_{r\theta}|_{r\to\infty} = -\sigma(\sin 2\theta)/2$, $\sigma_r|_{r\to(a+b)^+} = \sigma_r|_{r\to(a+b)^-}$, $\sigma_{r\theta}|_{r\to(a+b)^+} = \sigma_{r\theta}|_{r\to(a+b)^-}$, $u_r|_{r\to(a+b)^+} = u_r|_{r\to(a+b)^-}$, $u_\theta|_{r\to(a+b)^+} = u_\theta|_{r\to(a+b)^-}$, $\sigma_r|_{r\to a^+} = \sigma_r|_{r\to a^-}$, $\sigma_{r\theta}|_{r\to a^+} = \sigma_{r\theta}|_{r\to a^-}$, $u_r|_{r\to a^+} = u_r|_{r\to a^-}$, $u_\theta|_{r\to a^+} = u_\theta|_{r\to a^-}$, $u_r|_{r=0}$ = finite value and $u_\theta|_{r=\theta}$ = finite value.

Similarly, the twelve constants can be determined from boundary conditions and expressed in terms of material properties and microstructure geometries:

$$A_4 = -\sigma/4 \quad (5a)$$

$$B_4 = C_6 = D_6 = 0 \quad (5b)$$

$$A_5 = \frac{\sigma}{4}\frac{|N|}{|K|} \quad (5c)$$

$$B_5 = \frac{\sigma}{2(a+b)^2}\frac{|L|}{|K|} \quad (5d)$$

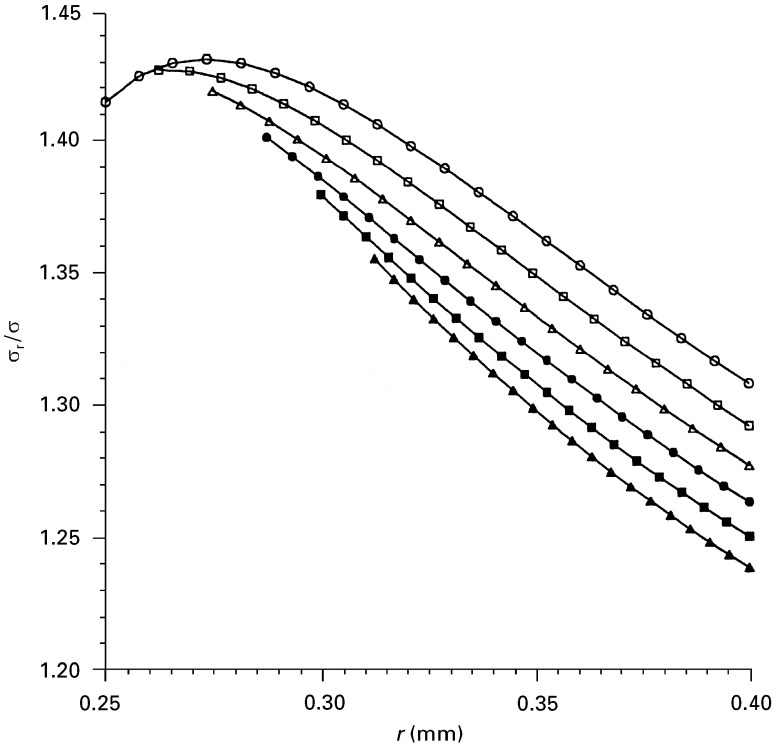

Figure 2 The variation of radial stresses near the porous interface for various ratios of b/a when $\theta = 0^\circ$ and $G^p/G^m = 0.6$. b/a: (○) 0%, (□) 5%, (△) 10%, (●) 15%, (■) 20%, (▲) 25%.

$$C_5 = \frac{\sigma}{4}\, a^3(a+b)\frac{|P|}{|K|} \tag{5e}$$

$$D_5 = \frac{\sigma}{2}\, a(a+b)\,\frac{|Q|}{|K|} \tag{5f}$$

$$A_6 = \frac{\sigma}{4}\frac{|N|}{|K|} + \frac{3}{a^4}\frac{\sigma}{4}\, a^3(a+b)\,\frac{|P|}{|K|} + \frac{\mathbf{2}}{a^2}\frac{\sigma}{2}\, a(a+b)\frac{|Q|}{|K|} \tag{5g}$$

$$B_6 = \frac{\sigma}{2(a+b)^2}\frac{|L|}{|K|} - \frac{2}{a^6}\frac{\sigma}{4}\, a^3(a+b)\,\frac{|P|}{|K|} - \frac{\sigma}{2a^3}\,(a+b)\frac{|Q|}{|K|} \tag{5h}$$

$$C_4 = -(a+b)^4\frac{\sigma}{4}\frac{|N|}{|K|} - \sigma(a+b)^4\frac{|L|}{|K|} + \frac{\sigma}{4}\, a^3(a+b)\frac{|P|}{|K|} - (a+b)^4\frac{\sigma}{4} \tag{5i}$$

$$D_4 = (a+b)^2\frac{\sigma}{2}\frac{|N|}{|K|} + \frac{3\sigma}{2}\,(a+b)^2\frac{|L|}{|K|} + \frac{\sigma}{2}\, a(a+b)\frac{|Q|}{|K|} + (a+b)^2\frac{\sigma}{2} \tag{5j}$$

where the determinants $|K|$, $|N|$, $|L|$, $|P|$ and $|Q|$ are a function of fibre radius, interface thickness, and elastic properties of fibre, porous interface and cement matrix as given in the Appendix.

The stress distributions near the fibre–cement interface for the dilute solution model subject to a transversely uniform tensile stress are the sum of those obtained separately from the two cases of angle-independent and angle-dependent applied stresses.

3. Effect of interfacial thickness and stiffness

Chen [13] developed a computer program based on the theoretical result of the three-phase model; the accuracy of the program was checked for the two special cases of $G^f = G^p = 0$ and $G^f = G^p = G^m$. The program is thus utilized to analyse numerically the effect of interfacial thickness and stiffness on the variation of radial and circumferential stresses near the porous interface between steel fibre and cement matrix. The interfacial thickness is empirically found to be roughly 40–60 μm [7] while the diameter of steel fibres is typically around 0.5 mm. Therefore, $a = 0.25$ mm and the interfacial thickness considered here is in the range of $0 \leqslant b/a \leqslant 0.25$. In addition, the shear modulus of a porous interface, G^p, should be lower than that of the bulk cement matrix, G^m. The shear modulus of steel fibre $G^f = 78$ GPa and the shear modulus of cement matrix $G^m = 10$ GPa are also assumed in the analysis.

The effect of interfacial thickness on the variations of radial ($\theta = 0^\circ$) and circumferential stresses ($\theta = 90^\circ$) near the steel fibre–cement interface, is studied first for the case of $G^p = 0.6G^m$. Fig. 2 shows the variation of radial stresses for six different interfacial thicknesses $b/a = 0\%, 5\%, 10\%, 15\%, 20\%$ and 25%, while Fig. 3 shows the variation of circumferential stresses. The interfacial thickness effect is also evaluated when $G^p = 0.8G^m$; the variations of resulting radial and circumferential stresses are presented in Figs 4 and 5, respectively.

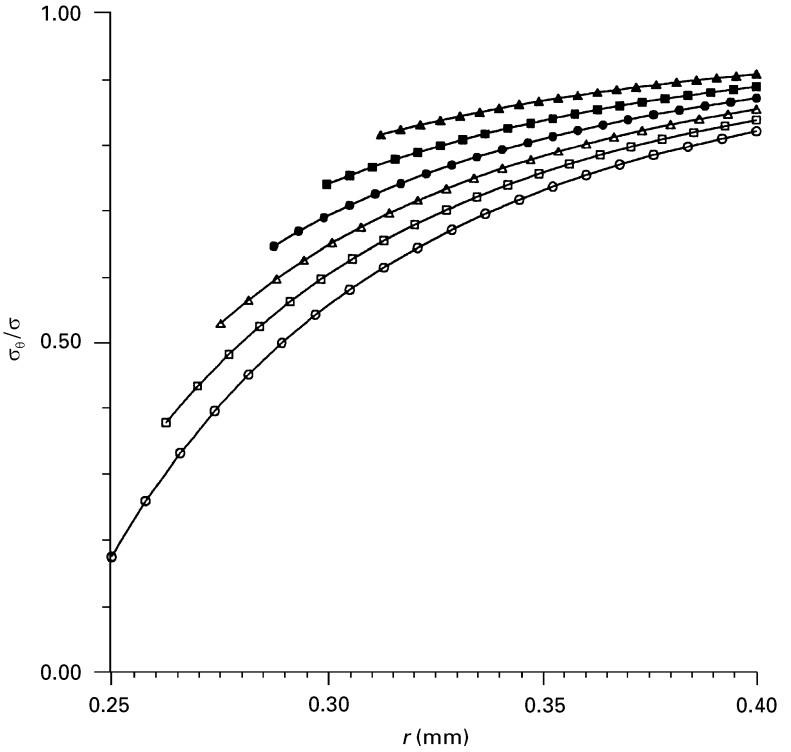

Figure 3 The variation of circumferential stresses near a porous interface for various ratios of b/a when $\theta = 90^\circ$ and $G^p/G^m = 0.6$. For key, see Fig. 2.

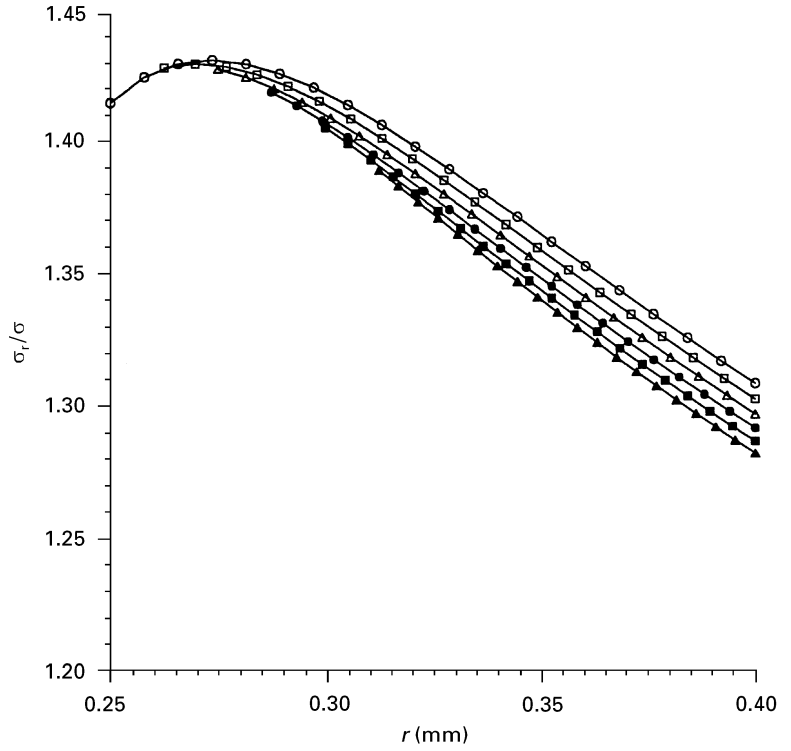

Figure 4 The variation of radial stresses near a porous interface for various ratios of b/a when $\theta = 0^\circ$ and $G^p/G^m = 0.8$. For key, see Fig. 2.

From Figs 2–5, it is found that either the maximum radial stress or the maximum circumferential stress will not occur on the boundary between steel fibre and cement matrix if the porous interface is absent, corresponding to the case of $b/a = 0$. Because the maximum radial and circumferential stresses occur within the cement matrix, brittle fracture is more likely to take place. As a result, the increase in both tensile strength and fracture toughness of the composite is insignificant. However, the failure mechanism of fibre reinforced cementitious composites can be altered if a porous interface is formed between steel fibre and cement matrix. It is seen that the maximum radial stress occurs on the boundary between porous interface and

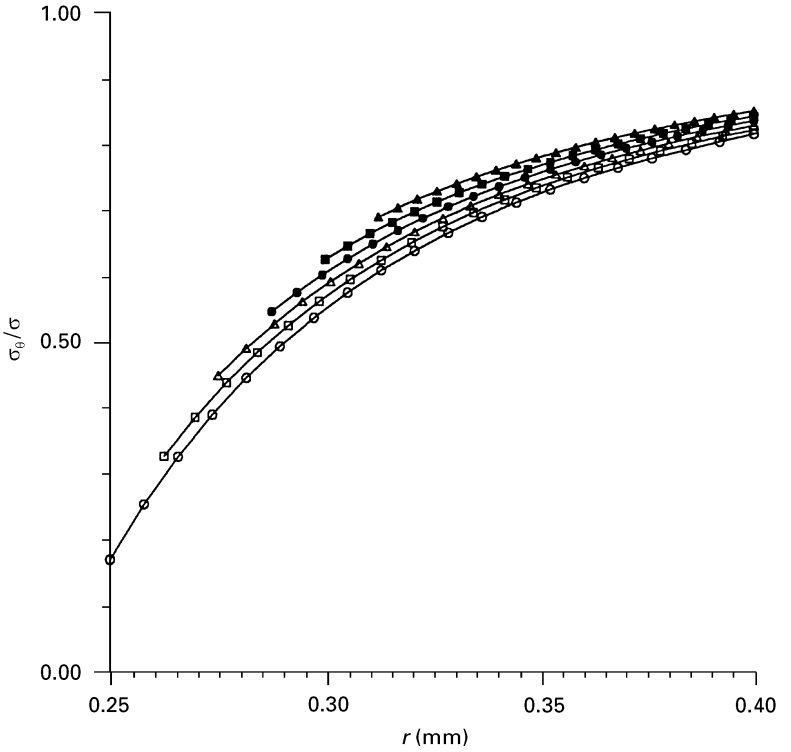

Figure 5 The variation of circumferential stresses near a porous interface for various ratios of b/a when $\theta = 90^\circ$ and $G^p/G^m = 0.8$. For key, see Fig. 2.

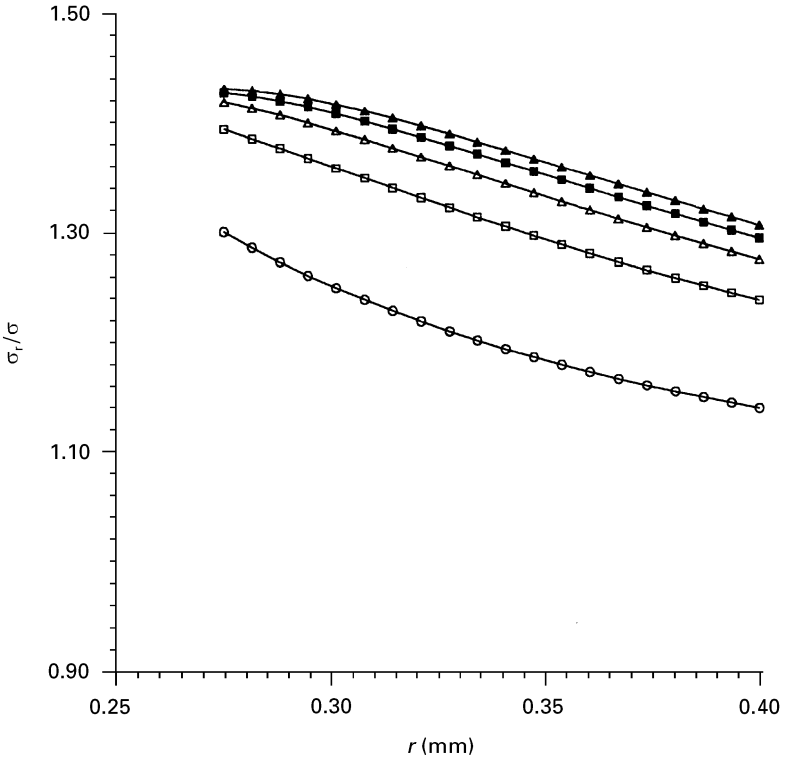

Figure 6 The variation of radial stresses near a porous interface for various ratios of G^p/G^m when $\theta = 0^\circ$ and $b/a = 10\%$. G^p/G^m: (○) 0.2, (□) 0.4, (△) 0.6, (■) 0.8, (▲) 1.0.

cement matrix from Figs 2 and 4. Also, the maximum radial stress decreases with increasing interfacial thickness for a specific interfacial stiffness. On the contrary, the maximum circumferential stress located at a distance far from the porous interface, increases with increasing interfacial thickness as shown in Figs 3 and 5.

Secondly, the effect of interfacial stiffness on the stress distributions near steel fibre–cement interface is evaluated for two cases of interfacial thicknesses. Fig. 6 shows the variation of radial stresses near the porous interface with a thickness of $b/a = 10\%$ for five interfacial stiffnesses $G^p/G^m = 0.2$, 0.4, 0.6, 0.8 and 1.0, while Fig. 7 shows the variation of circumferential

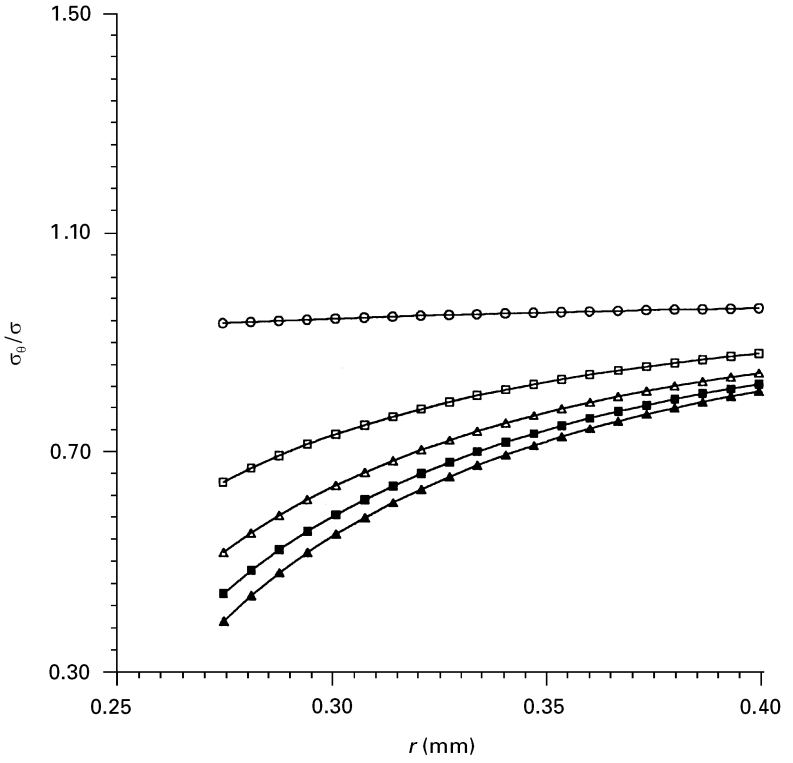

Figure 7 The variation of circumferential stresses near a porous interface for various ratios of G^p/G^m when $\theta = 90^\circ$ and $b/a = 10\%$. For key, see Fig. 6.

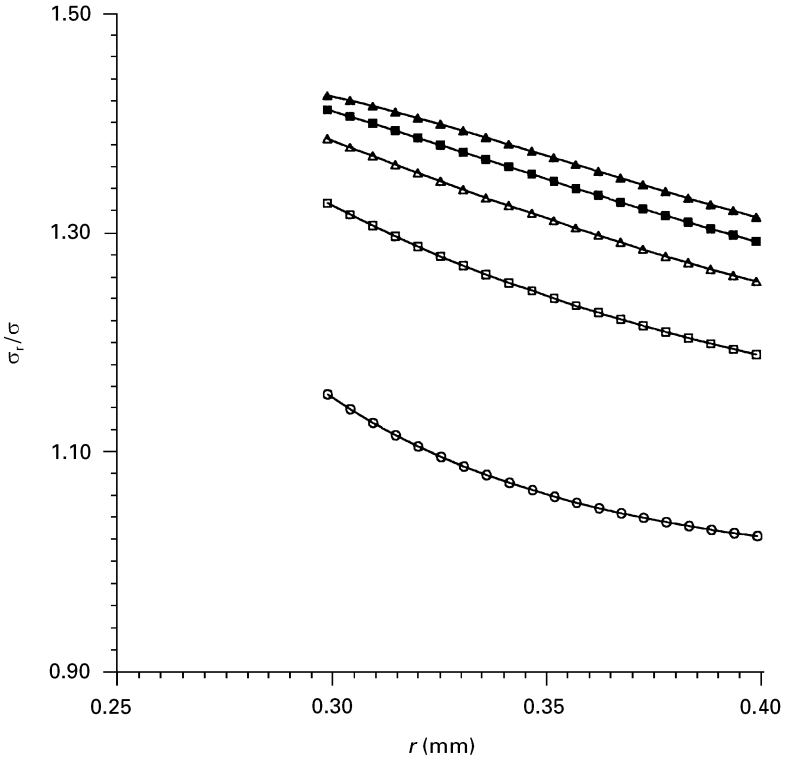

Figure 8 The variation of radial stresses near a porous interface for various ratios of G^p/G^m when $\theta = 0^\circ$ and $b/a = 20\%$. For key, see Fig. 6.

stresses. For $b/a = 20\%$, the radial and circumferential stresses are shown in Figs 8 and 9, respectively. From Figs 6 and 8, it is found that the maximum radial stress occurs on the boundary of porous interface and cement matrix. Meanwhile, the maximum radial stress increases with increasing interfacial stiffness. However, the maximum circumferential stress, as shown in Figs 7 and 9, occurs within the cement matrix, except for the case for $b/a = 20\%$ and $G^p/G^m = 0.2$. The actual location of the maximum circumferential stress depends on the magnitude of interfacial stiffness; the maximum circumferential stress decreases with increasing interfacial stiffness.

Based on the results of the analysis for steel fibre-reinforced cementitious composites with various interfacial thicknesses and stiffnesses, it is found that the

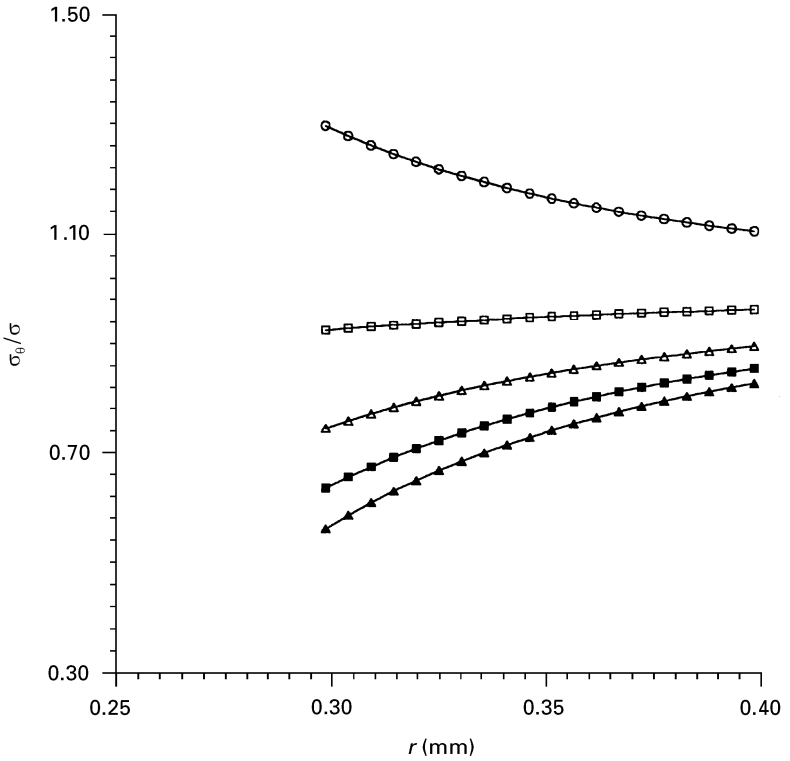

Figure 9 The variation of circumferential stresses near a porous interface for various ratios of G^p/G^m when $\theta = 90^\circ$ and $b/a = 20\%$. For key, see Fig. 6.

stress distributions depend on the presence of a porous interface. When there is no porous interface, which can be accomplished by adding adequate pozzolanic materials into a slurry of cement and steel fibres, the maximum radial and circumferential stresses occur somewhere within the cement matrix. It is expected that microcracks might initiate and propagate from the cement matrix, giving a brittle fracture failure. On the other hand, the presence of a porous interface will produce higher radial stresses near the fibre–cement interface. In most cases, the adhesive strength of the porous interface is lower than the cohesive strength of the cement matrix. As a result of that, microcracks might initiate and propagate initially along the steel fibre–cement interface. To some extent, the microcracks will deflect and coalescence with other pre-existing macrocracks. The failure mechanism in steel fibre-reinforced cementitious composites with a porous interface, which is different from that without a porous interface, will consume a large amount of energy during the process of crack propagation, giving a higher value of fracture toughness.

4. Discussion

Based on the modelling results, it is known that the maximum radial and circumferential stresses near a porous interface are affected by interfacial thickness and stiffness. The maximum radial stress decreases with increasing interfacial thickness, but the maximum circumferential stress increases with increasing interfacial thickness. Also, the maximum radial stress is reduced but the maximum circumferential stress is increased if interfacial stiffness is decreased. Presumably the composite strength is expected to increase because the presence of a porous interface reduces the magnitude of the radial stress, causing interface failure, as compared to the case with a stiffer interface or no interface at all. Therefore, there is an optimum interfacial thickness and stiffness with which the magnitude of the maximum radial stress is reduced but is still larger than the maximum circumferential stress, leading to a failure mechanism of interface debonding and fibre pull-out. The strength and toughness of a fibre-reinforced cementitious composite, having the optimum interfacial thickness and stiffness, can be improved.

The ratio of the maximum circumferential stress within the cement matrix to the maximum radial stress on the boundary between a porous interface and a cement matrix, is shown in Fig. 10 for various interfacial thicknesses and stiffnesses. From Fig. 10, it is found that the maximum radial stress on the boundary between a porous interface and a cement matrix is higher than the maximum circumferential stress within the cement matrix for most cases discussed here. The maximum circumferential stress within the cement matrix will not exceed the maximum radial stress on the boundary between a porous interface and a cement matrix unless the interfacial stiffness is very low. In practice, the tensile strength of the cement paste is larger than the tensile strength on the boundary between a porous interface and a cement matrix. As a result of that, the failure mechanism of interface debonding and fibre pull-out occurs, consuming a large amount of energy during the process of crack propagation and increasing the toughness of fibre-reinforced cementitious composites.

Similarly, the ratios of the maximum circumferential stress within the cement matrix to the maximum radial stress on the boundary between the porous interface and cement matrix for cementitious composites with carbon, glass or polypropylene fibres, are shown in Figs 11–13,

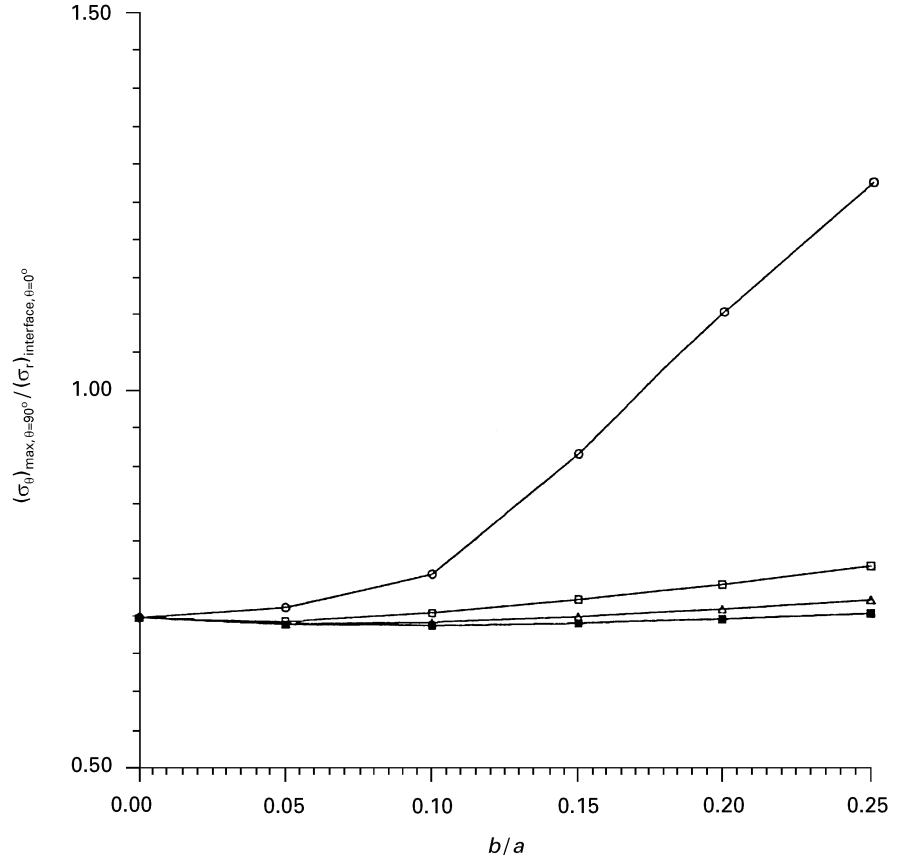

Figure 10 The ratio of the maximum circumferential stress within the cement matrix to the maximum radial stress on the boundary between a porous interface and a cement matrix in steel fibre-reinforced cementitious composites. G^p/G^m: (○) 0.2, (□) 0.4, (△) 0.6, (■) 0.8.

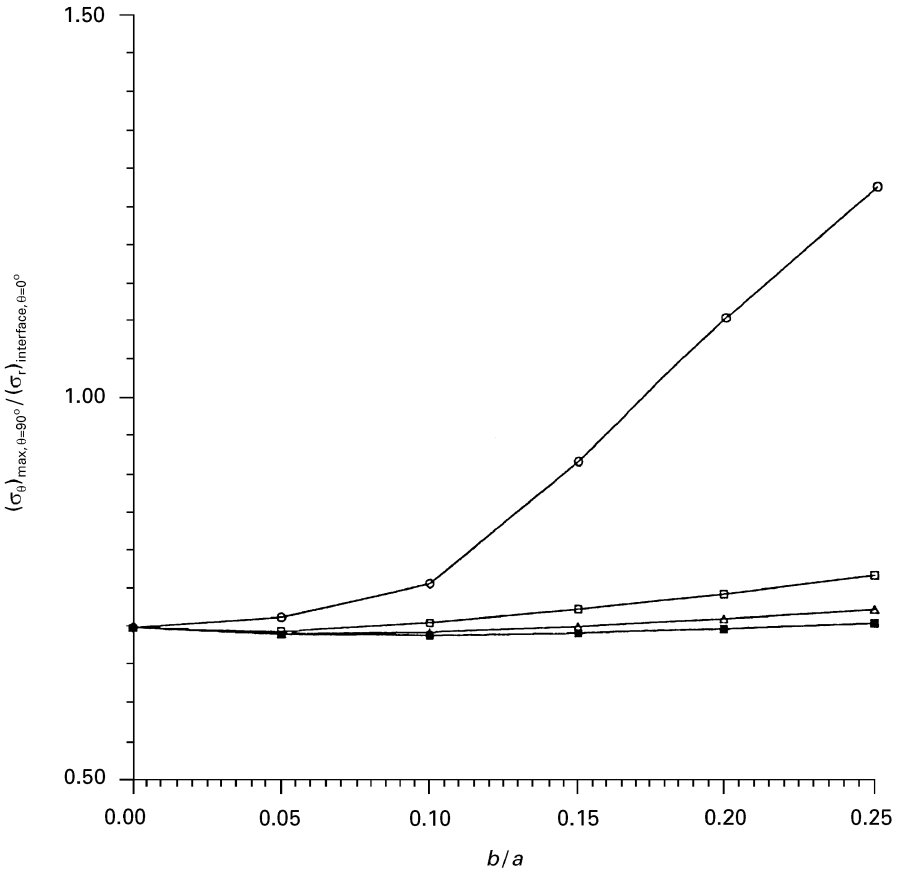

Figure 11 The ratio of the maximum circumferential stress within the cement matrix to the maximum radial stress on the boundary between a porous interface and a cement matrix in carbon fibre-reinforced cementitious composites. For key, see Fig. 10.

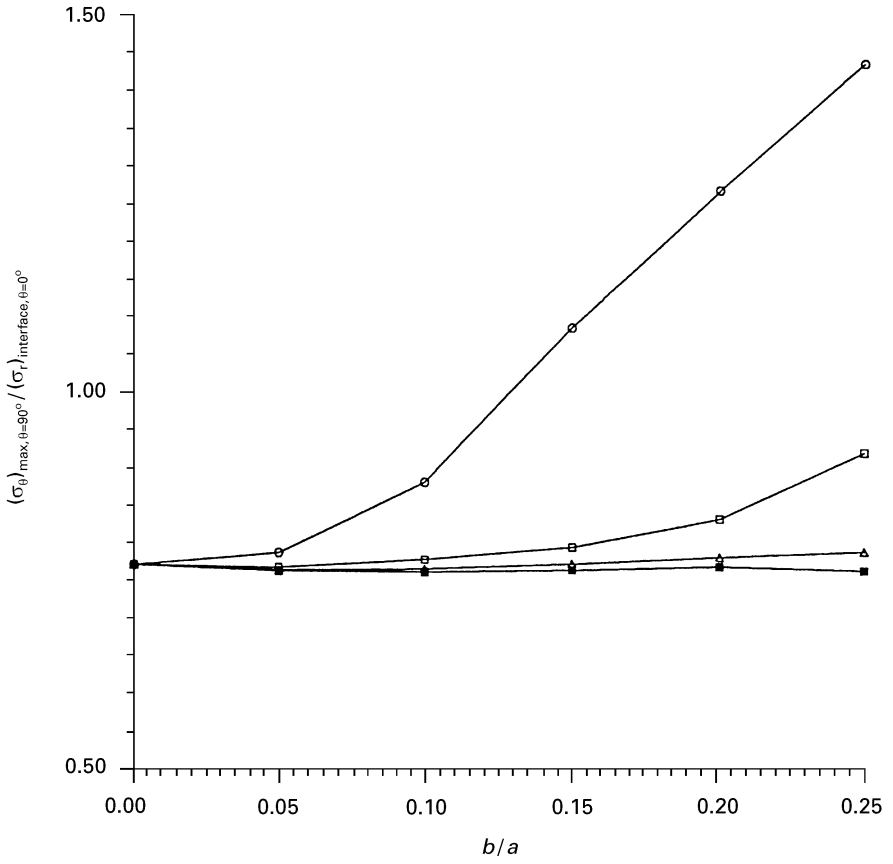

Figure 12 The ratio of the maximum circumferential stress within the cement matrix to the maximum radial stress on the boundary between a porous interface and a cement matrix in glass fibre-reinforced cementitious composites. For key, see Fig. 10.

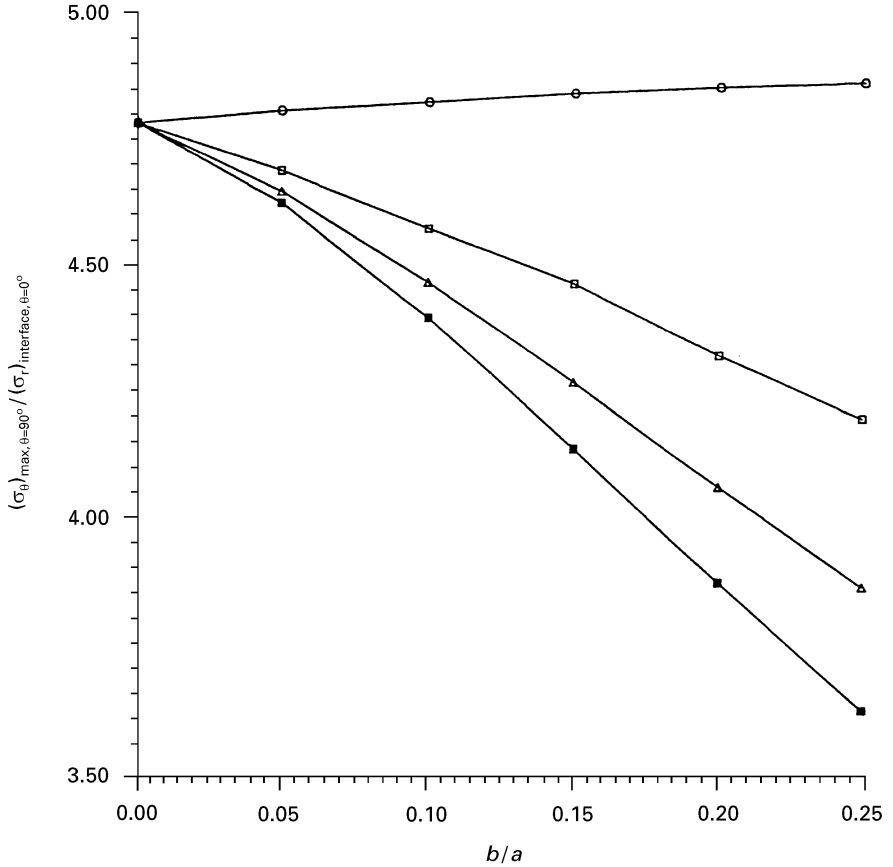

Figure 13 The ratio of the maximum circumferential stress within the cement matrix to the maximum radial stress on the boundary between a porous interface and a cement matrix in polypropylene fibre-reinforced cementitious composites. For key, see Fig. 10.

respectively. It is seen that steel, carbon and glass fibres have a similar reinforcement effect on the stress distributions near the fibre–cement interface, except polypropylene fibres. The maximum circumferential stress within the cement matrix could be five times the maximum radial stress on the boundary between a porous interface and a cement matrix for polypropylene fibre-reinforced cementitious composites. Therefore, microcracks might initiate and propagate from the cement matrix instead of the porous interface, leading to a brittle fracture.

Polypropylene fibres (modulus of elasticity $E = 5$ GPa) are more compliant than steel ($E = 200$ GPa), carbon ($E = 230$ GPa) and glass fibres ($E = 80$ GPa). Hence, it can be said that fibres with higher elastic moduli are preferred in fibre-reinforced cementitious composites when the failure mechanism of interfacial debonding and fibre pull-out is pursued. As a rule of thumb, the criterion for the occurrence of interface debonding and fibre pull-out is

$$\frac{(\sigma_\theta)_{\max,\theta=90^\circ}}{(\sigma_r)_{\text{interface},\theta=0^\circ}} \leqslant \frac{\sigma_{\text{cohesive}}}{\sigma_{\text{adhesive}}} \tag{6}$$

where σ_{cohesive} is the cohesive strength of the cement matrix, and σ_{adhesive} is the adhesive strength between fibre and cement matrix. Once σ_{cohesive} and σ_{adhesive} are determined experimentally, the results shown in Figs 10–13 can be employed to determine if the failure mechanism of interface debonding and fibre pull-out is more likely to happen.

5. Conclusions

Based on the results of a dilute solution model subject to a transversely uniform tensile stress, it was found that the stress distributions near the fibre–cement matrix interface are affected by interfacial thickness and stiffness. When there is no porous interface introduced between fibre and cement matrix, the maximum stress occurs within the cement matrix, resulting in a brittle fracture failure. However, the maximum radial stress occurs on the boundary between the porous interface and the cement matrix if a porous interface is present. As a result, microcracks might initiate and propagate along the porous interface, giving a higher fracture toughness in fibre-reinforced cementitious composites.

The maximum radial stress near porous interfaces decreases with increasing interfacial thickness but with decreasing interfacial stiffness, while the maximum circumferential stress increases with increasing interfacial thickness but with decreasing interfacial stiffness. Optimum interfacial thickness and stiffness, with which the maximum radial stress on the boundary between the porous interface and the cement matrix is reduced but is still higher than the maximum circumferential stress within the cement matrix, have been evaluated for various reinforcements, including steel, carbon, glass and polypropylene fibres. Once the cohesive strength of the cement matrix and the adhesive strength between the porous interface and the cement matrix are found experimentally, the theoretical results can be used to determine if the failure mechanism of interfacial debonding and fibre pull-out is more likely to occur.

Acknowledgement

The financial support of the National Science Council, Taiwan under contracts NSC 82-0410-E006-326 and NSC 82-0618-E006-327 is gratefully acknowledged.

References

1. J. AVESTON, G. A. COOPER and A. KELLY "The properties of fiber composites", Conference Proceedings National Physical Laboratory, (I.P.C. Science and Technology Press, UK 1971).
2. V. S. RAMACHANDRAN, R. F. FELDMAN and J. J. BEAUDOIN "Concrete science – treatise of current research" (Heyden, PA, USA 1981).
3. A. BENTUR, S. DIAMOND and S. MINDESS, *J. Mater. Sci.* **20** (1985) 3610.
4. S. MINDESS and J. F. YOUNG, "Concrete" (Prentice-Hall, Englewood Cliffs, NJ, 1981).
5. A. BENTUR, S. DIAMOND and S. MINDESS, *Cem. Concr. Res.* **15** (1985) 331.
6. S. WEI, J. A. MANDEL and S. SAID, **ACI J. 83** (1986) 597.
7. A. BENTUR, *Adv. Cementit. Mater. Ceram. Trans.* **16** (1990) 523.
8. M. KAWAMURA and S. IGARASHI, *J. Mater. Civil Eng. ASCE* **4** (1992) 227.
9. K. H. LO, R. W. SCHMITZ and W. G. GOTTENBERG, *Mater. Res. Soc. Symp. Proc.* **170** (1990) 55.
10. L. MONETTE, M. P. ANDERSON and G. S. GREST, *J. Mater. Sci.* **28** (1993) 79.
11. R. M. CHRISTENSEN, "Mechanics of composite materials" (Wiley, New York 1981).
12. S. P. TIMOSHENKO and J. N. GOODIER, "Theory of elasticity" (McGraw Hill, New York 1970).
13. M. T. CHEN, Master Thesis, Department of Civil Engineering, National Cheng Kung University, Tainan, Taiwan (1994).

Received 19 April 1996
and accepted 18 April 1997

Appendix: The determinants |K|, |N|, |L|, |P| and |Q|

$$|K| = \begin{vmatrix} (3-4\nu^m)\beta+1 & (8-12\nu^m)\beta+4\nu^p & \alpha^3(\beta-1) & \alpha[(4-4\nu^m)\beta-(4-4\nu^p)] \\ (4\nu^m-3)\beta-1 & (12\nu^m-10)\beta-(6-4\nu^p) & \alpha^3(\beta-1) & -\alpha[(2-4\nu^m)\beta-(2-4\nu^p)] \\ \alpha(\delta-1) & \alpha^3(4\nu^f\delta-4\nu^p) & (3-4\nu^f)\delta+1 & (4-4\nu^f)\delta+(4-4\nu^p) \\ \alpha(1-\delta) & -\alpha^3[(6-4\nu^f)\delta-(6-4\nu^p)] & (3-4\nu^f)\delta+1 & (2-4\nu^f)\delta-(2-4\nu^p) \end{vmatrix} \tag{A1}$$

$$|N| = \begin{vmatrix} -(4-4\nu^{m})\beta & (8-12\nu^{m})\beta+4\nu^{p} & \alpha^{3}(\beta-1) & \alpha[(4-4\nu^{m})\beta-(4-4\nu^{p})] \\ (4-4\nu^{m})\beta & (12\nu^{m}-10)\beta-(6-4\nu^{p}) & \alpha^{3}(\beta-1) & -\alpha[(2-4\nu^{m})\beta-(2-4\nu^{p})] \\ 0 & \alpha^{3}(4\nu^{f}\delta-4\nu^{p}) & (3-4\nu^{f})\delta+1 & (4-4\nu^{f})\delta+(4-4\nu^{p}) \\ 0 & -\alpha^{3}[(6-4\nu^{f})\delta-(6-4\nu^{p})] & (3-4\nu^{f})\delta+1 & (2-4\nu^{f})\delta-(2-4\nu^{p}) \end{vmatrix} \tag{A2}$$

$$|L| = \begin{vmatrix} (3-4\nu^{m})\beta+1 & (4\nu^{m}-4)\beta & \alpha^{3}(\beta-1) & \alpha[(4-4\nu^{m})\beta-(4-4\nu^{p})] \\ (4\nu^{m}-3)\beta-1 & (4-4\nu^{m})\beta & \alpha^{3}(\beta-1) & -\alpha[(2-4\nu^{m})\beta-(2-4\nu^{p})] \\ \alpha(\delta-1) & 0 & (3-4\nu^{f})\delta+1 & (4-4\nu^{f})\delta+(4-4\nu^{p}) \\ \alpha(1-\delta) & 0 & (3-4\nu^{f})\delta+1 & (2-4\nu^{f})\delta-(2-4\nu^{p}) \end{vmatrix} \tag{A3}$$

$$|P| = \begin{vmatrix} (3-4\nu^{m})\beta+1 & (8-12\nu^{m})\beta+4\nu^{p} & (4\nu^{m}-4)\beta & \alpha[(4-4\nu^{m})\beta-(4-4\nu^{p})] \\ (4\nu^{m}-3)\beta-1 & (12\nu^{m}-10)\beta-(6-4\nu^{p}) & (4-4\nu^{m})\beta & -\alpha[(2-4\nu^{m})\beta-(2-4\nu^{p})] \\ \alpha(\delta-1) & \alpha^{3}(4\nu^{f}\delta-4\nu^{p}) & 0 & (4-4\nu^{f})\delta+(4-4\nu^{p}) \\ \alpha(1-\delta) & -\alpha^{3}[(6-4\nu^{f})\delta-(6-4\nu^{p})] & 0 & (2-4\nu^{f})\delta-(2-4\nu^{p}) \end{vmatrix} \tag{A4}$$

$$|Q| = \begin{vmatrix} (3-4\nu^{m})\beta+1 & (8-12\nu^{m})\beta+4\nu^{p} & \alpha^{3}(\beta-1) & (4\nu^{m}-4)\beta \\ (4\nu^{m}-3)\beta-1 & (12\nu^{m}-10)\beta-(6-4\nu^{p}) & \alpha^{3}(\beta-1) & (4-4\nu^{m})\beta \\ \alpha(\delta-1) & \alpha^{3}(4\nu^{f}\delta-4\nu^{p}) & (3-4\nu^{f})\delta+1 & 0 \\ \alpha(1-\delta) & -\alpha^{3}[(6-4\nu^{f})\delta-(6-4\nu^{p})] & (3-4\nu^{f})\delta+1 & 0 \end{vmatrix} \tag{A5}$$

where $\alpha = a/(a+b)$, $\beta = G^{p}/G^{m}$ and $\delta = G^{p}/G^{f}$.